This article has been accepted for publication in IEEE Journal of Selected Topics in Applied Earth Observations and Remote Sensing. This is the author's version which has not been fully e
content may change prior to final publication. Citation information: DOI 10.1109/JSTARS.2023.3258059

Machine Learning Approaches for Road Condition Monitoring Using Synthetic Aperture Radar

Lucas Germano Rischioni, Arun Babu, *Graduate Student Member, IEEE*, Stefan V. Baumgartner, *Senior Member, IEEE*, and Gerhard Krieger, *Fellow, IEEE*

***Abstract*—Airborne Synthetic Aperture Radar (SAR) has the potential to monitor remotely the road traffic infrastructure on a large scale. Of particular interest is the road surface roughness, which is an important road safety parameter. For this task, novel algorithms need to be developed. Machine learning approaches, such as Artificial Neural Networks (ANN) and Random Forest Regression, which can perform non-linear regression, can achieve this goal. This work considers fully polarimetric airborne radar datasets captured with DLR's airborne F-SAR radar system. Several machine learning-based approaches were tested on the datasets to estimate road surface roughness. The resulting models were then compared with ground truth surface roughness values and also with the semi-empirical surface roughness model studied in previous work.**

***Index Terms*—Synthetic aperture radar, additive noise, surface roughness, machine learning, vehicle safety.**

I. Introduction

ROADS contribute crucially to the development and economic growth of a country, being responsible for bringing several social benefits [1], [2]. They provide access to different regions of the country and promote economic and social development [3], [4]. Therefore, monitoring the quality of road infrastructure and carrying out regular maintenance are equally important for a country's economy and also for the safety of road users. There are several factors that affect the road surface quality, of which one important is the road surface roughness [5]. This is because the road surface roughness is responsible for the friction between the road surface and the tires of the vehicles [6], [7]. A sufficient level of friction is required for safe acceleration, steering, and braking of the vehicles [8]. If the friction is below the required level, this may cause the vehicle to skid [9], and if the friction is very high, this can result in increased fuel consumption, tire abrasion, noise, etc [10]. Although traffic accidents can occur for a variety of reasons, several studies have shown that poor 'skid resistance' increases the probability of an accident [8]. Therefore, regular inspection of the road surface is necessary to ensure that the roughness values of the road surface are within optimal limits, which in turn can help to reduce the number of road accidents.

At present, road conditions in Germany are measured in average once every 4 years by special survey vehicles equipped with various measuring devices driving over motorways and other major roads [11], [12]. The deterioration of the road surface occurs mainly in the winter season due to repeated freeze-thaw cycles [13]. This highlights the need to monitor the condition of the road surface more frequently, preferably annually. However, with the need for survey vehicles, this requires a lot of personnel and it is generally a costly and time-consuming procedure [12].

SAR remote sensing can be considered as an alternative approach for wide-scale road surface roughness monitoring because it is sensitive to changes in dielectric values and roughness of the surface under observation [14]. In addition, SAR offers high spatial resolution, day-night, and cloud penetration capabilities [15]. It is widely used to estimate soil roughness of agricultural fields [16]. SAR polarimetry-based methods, SAR backscattering-based semi-empirical models, and physical models have been developed to estimate soil moisture and soil roughness [17]–[20]. However, these models cannot be used to estimate road surface roughness. Because the road surfaces have completely different characteristics from the conditions assumed in the development of these models. Road surfaces are smoother and roughness is expected to be only in the millimeter range (1 to 3 mm) [5] and the signal-to-noise ratio (SNR) expected from a smooth road surface is much lower compared to the rough agricultural fields. Also, asphalt and concrete, which are commonly used for road construction, have a completely different dielectric constant than the agricultural fields [14].

A few studies can be found in the literature that utilizes the SAR datasets for road surface quality monitoring. In [21], the spaceborne L-band ALOS-PALSAR datasets with 7 m spatial resolution were used to map the relationship between the SAR backscatter values and the international roughness index (IRI) values of the roads in Thailand. The IRI is a widely used parameter to indicate the unevenness of the road surface [22]. A similar study can be found in [23], where the spaceborne X-band Cosmo-SkyMed SAR datasets with 3 m spatial resolution were used to derive the IRI of the roads in the Commonwealth of Virginia, USA. However, both of the above-mentioned studies used medium-resolution SAR datasets and did not produce a road surface roughness image that a road maintenance engineer without SAR knowledge could use to identify problematic areas on the road. One study that produced road surface roughness images can be found in [24]. In [24], the authors used high-resolution airborne X-band SAR datasets with 25 cm spatial resolution acquired by the F-SAR sensor of the German Aerospace Center (DLR).

Lucas Germano Rischioni was with the Microwaves and Radar Institute, German Aerospace Center (DLR), 82234 Weßling, Germany. He is now with the Aeronautical Technological Institute (ITA), São José dos Campos - SP, 12228-900, Brazil (email: lucasgrischioni@gmail.com). Arun Babu, Stefan V. Baumgartner, and Gerhard Krieger are with the Microwaves and Radar Institute, German Aerospace Center (DLR), 82234 Weßling, Germany (email: arun.babu@dlr.de; stefan.baumgartner@dlr.de; gerhard.krieger@dlr.de).

This work is licensed under a Creative Commons Attribution 4.0 License. For more information, see https://creativecommons.org/licenses/by/4.0/

This article has been accepted for publication in IEEE Journal of Selected Topics in Applied Earth Observations and Remote Sensing. This is the author's version which has not been fully c
content may change prior to final publication. Citation information: DOI 10.1109/JSTARS.2023.3258059

They developed a semi-empirical model that generated the surface roughness images as a function of incidence angle and backscatter values. It is interesting to investigate how well state-of-the-art machine learning models, that can learn and adapt to the statistics of the data [25], can estimate the road surface roughness.

This study evaluates the potential of machine learning models for estimating road surface roughness using high-resolution airborne polarimetric SAR datasets and then producing a road surface roughness image for the end user. Considering the difficulty of obtaining ground truth data from busy roads to train the models and validate the results, special attention was given to develop a methodology to properly train machine learning models with a small set of ground truth data.

The rest of this article is organized in the following order. Details about the test sites considered in this study are given in Section II. Section III provides information about the airborne SAR datasets and the ground truth data used. The methodology used to estimate the road surface roughness using the machine learning models is explained in Section IV. The experimental results are presented and discussed in detail in Section V. Section VI concludes this article.

II. Test Sites

The test sites must contain road surfaces made of different materials such as concrete and asphalt with different surface roughness values. Three such test sites were identified and used for this study.

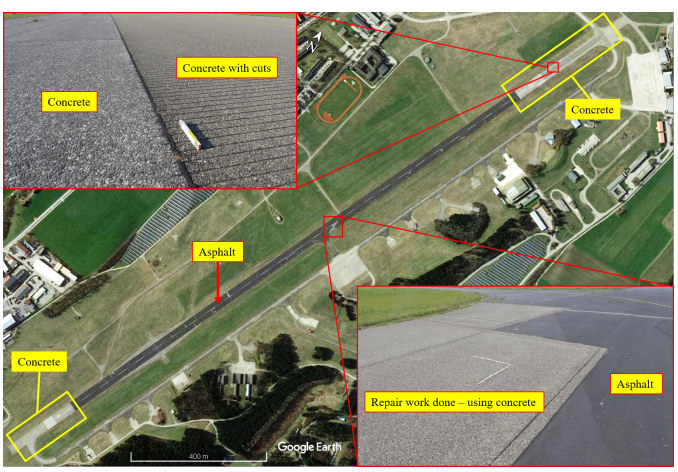

Fig. 1. Primary test site - Kaufbeuren airfield.

The primary test site is the Kaufbeuren airfield in Bavaria, Germany. It is a former military airfield that contains runways, taxiways, and parking areas. The Google Earth image of the test site is shown in Fig. 1. It can be seen that the two ends of the runway are concrete, as indicated by the yellow rectangles, and that the part of the runway between these concrete ends is asphalt. The photo on the upper left side of Fig. 1 shows an area of the concrete patch where both smooth concrete and concrete regions with repeated cuts are present. Similarly, the photo on the lower right side of Fig. 1 shows an asphalt area in the middle of the runway where repair works were done with concrete. The availability of smooth, rough, and cracked surfaces made of different materials makes Kaufbeuren airfield a perfect test site for this study. In addition, ground truth (GT) surface roughness values were collected at this test site, which are used to train the machine learning models and validate the results estimated using these models. The details of the GT data collection are discussed in the next section.

As secondary test sites for this study, the "Demonstrations-, Untersuchungs- und Referenzareal der BASt (duraBASt)" [26] test site in Cologne, and the Wolfsburg motorway intersection at Braunschweig, both in Germany were considered. Fig. 2(a) shows the Google Earth image of the duraBASt test site, which is marked with the yellow ellipse in the zoomed view. It can be seen that the different regions of the duraBASt test site consist of materials with different colors, indicating a different material composition and thus, different surface roughness values. Fig. 2(b) shows the Google Earth image of the Wolfsburg motorway intersection. It can be seen that this test area consists of long highways and a uniform surface roughness is expected here. However, in the zoom view, a sudden change in the color of the highway surface can be seen, indicating a change in surface roughness. This may be due to a repair where an asphalt mix with a different material composition was used. Unfortunately, no GT data are available for the secondary test sites. Therefore, the surface roughness results obtained from these test sites can only be compared to the results obtained from the surface roughness estimation models investigated in previous work [5], [24], [27].

III. Datasets

The details about the airborne SAR datasets and the ground truth data used in this study are discussed in this section.

A. Airborne SAR datasets

In this study, fully polarimetric X-band data acquired with DLR's airborne F-SAR sensor [28] were used to investigate road roughness at the three different test sites. Table I shows the major F-SAR parameters used during data acquisition.

TABLE I
Summary of the F-SAR instrument properties [29]

Frequency band	X-band
Frequency (GHz)	9.6
Bandwidth (MHz)	760
Pulse Repetition Frequency (kHz)	1.2
Range resolution (m)	0.25
Azimuth resolution (m)	0.25

The primary data used in this work comprise eleven fully polarimetric SAR (PolSAR) datasets from the Kaufbeuren test site. Each of these datasets was acquired in September 2020 with different flight directions and incidence angles, allowing different views of the runway, taxiway, and parking area at Kaufbeuren, thus contributing to the diversification of the data. Table II shows information about the F-SAR datasets acquired from the Kaufbeuren test site. In addition, datasets were collected for the duraBASt test in September 2019 and for the Braunschweig test site in August 2020. All of these datasets were acquired on dry, sunny days to avoid backscatter

This work is licensed under a Creative Commons Attribution 4.0 License. For more information, see https://creativecommons.org/licenses/by/4.0/

This article has been accepted for publication in IEEE Journal of Selected Topics in Applied Earth Observations and Remote Sensing. This is the author's version which has not been fully c
content may change prior to final publication. Citation information: DOI 10.1109/JSTARS.2023.3258059

(a) (b)

Fig. 2. Secondary test sites. (a) duraBASt test site. (b) Wolfsburg motorway intersection, Braunschweig.

variations due to rainwater filling the voids or cracks on the road surface.

TABLE II
INFORMATION ABOUT THE F-SAR DATASETS ACQUIRED FROM THE KAUFBEUREN TEST SITE

Dataset ID	Incidence angle at the runway	Flight track w.r.t. runway	Flight heading angle	Used for
PS02	23° to 51°	45°	91.18°	Train
PS03	29° to 55°	45°	91.20°	Test
PS04	30° approx.	Parallel	201.71°	Train
PS05	32° to 55°	Across	291.69°	Train
PS06	32° approx.	Parallel	21.70°	Train
PS08	35° approx.	Parallel	201.72°	Train
PS10	34° approx.	Parallel	21.70°	Train
PS11	39° approx.	Parallel	201.71°	Test
PS12	40° approx.	Parallel	21.70°	Train
PS13	45° approx.	Parallel	201.72°	Train
PS14	45° approx.	Parallel	21.70°	Test

B. Ground truth data collection

GT surface roughness values were collected from the Kaufbeuren test site to train the machine learning-based surface roughness estimation models and also to validate the surface roughness values estimated using the F-SAR datasets.

In total ten 1 m² spots on the Kaufbeuren runway and taxiway were chosen as the GT spots (cf. Fig. 3). The GT spots were spread across the smooth, rough, and cracked asphalt and concrete surfaces of the runway, taxiway, and parking area. A handheld laser scanner was used to collect the GT data. This scanner was able to measure the vertical surface undulation of the surface with an accuracy of 0.025 mm.

Fig. 4(a) shows the GT data collection activity using the handheld laser scanner for the GT spot 1 and Fig. 4(b) shows the surface undulation image generated for the same spot using the data acquired by the laser scanner. The surface undulation values measured for each GT spot were then used to calculate a single ground truth surface roughness value (GT h_{rms}) using the following equation:

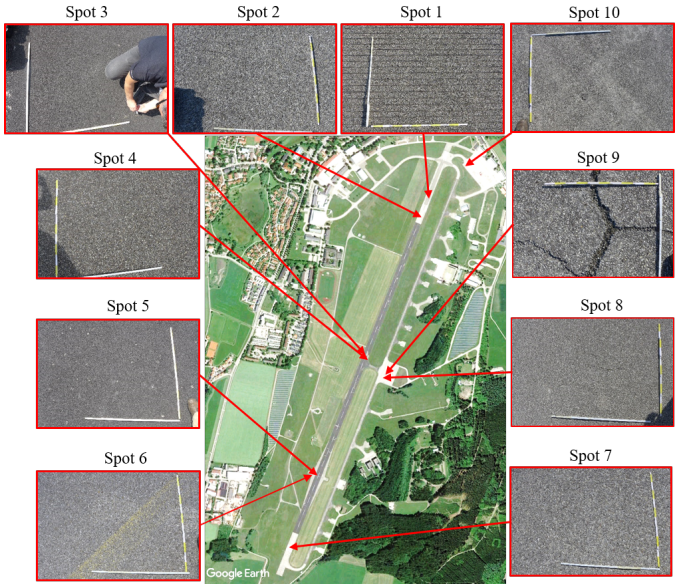

Fig. 3. Kaufbeuren test site, with emphasis on its ten ground-truth spots.

$$h_{rms} = \sqrt{\frac{\sum_{i=1}^{n}(h_i - \overline{h})^2}{n-1}}, \quad (1)$$

where h_{rms} is the root mean square (RMS) height commonly used to characterize vertical surface roughness [17], h_i is the surface undulation value measured for the ith sample, $\overline{h}$ is the mean of all the samples and n is the number of samples.

Table III shows information about minimum and maximum surface undulations measured at each of the GT spots, the GT h_{rms} values estimated using (1) and the characteristics of the GT spots.

IV. METHODOLOGY

To determine the road surface roughness, the h_{rms} parameter must be estimated. However, it is not possible to estimate h_{rms} directly from the SAR data. Fortunately, the effective

This work is licensed under a Creative Commons Attribution 4.0 License. For more information, see https://creativecommons.org/licenses/by/4.0/

This article has been accepted for publication in IEEE Journal of Selected Topics in Applied Earth Observations and Remote Sensing. This is the author's version which has not been fully e
content may change prior to final publication. Citation information: DOI 10.1109/JSTARS.2023.3258059

(a)

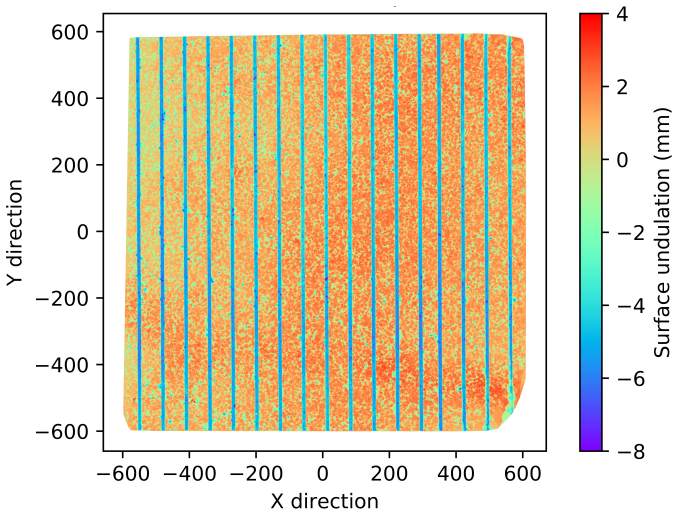

(b)

Fig. 4. (a) GT data collection process. (b) Surface undulation image for GT spot 1, which is the only spot that contains periodically repeated cuts.

TABLE III
INFORMATION ABOUT THE GROUND TRUTH SPOTS

GT spot	Surface undulation [mm]		GT h_{rms}	Characteristics
	Min	Max		
1	-7.09	2.73	2.36	Concrete area with repeated cuts
2	-3.00	2.27	0.99	Smooth concrete area
3	-2.53	1.70	0.66	Smooth asphalt area
4	-4.34	1.66	0.88	Smooth area- repair work done using concrete
5	-2.45	2.26	0.68	Smooth asphalt area
6	-4.14	2.01	0.98	Smooth concrete area
7	-3.03	2.62	1.09	Smooth concrete area
8	-2.38	1.91	0.61	Concrete, very smooth
9	-13.07	4.25	2.86	Area with deep and non-oriented cracks
10	-5.82	1.92	0.76	Concrete, very smooth

vertical surface parameter (ks) can be estimated from the SAR data. The parameter ks is unitless and given as in [17]

$$ks = (2\pi/\lambda_c)h_{rms}, \tag{2}$$

where λ_c is the wavelength of the SAR system. For the X-band F-SAR system with 9.6 GHz carrier frequency, the value of λ_c is 3.12 cm. After estimating ks from the SAR data, (2) can be easily inverted to calculate h_{rms}. This section describes the methodology used to train the machine learning-based models and to estimate ks from the F-SAR datasets.

A. PolSAR Data Preprocessing

Before extracting the features that were used as input to the machine learning models, it is necessary to preprocess the data obtained from F-SAR. The block diagram shown in Fig. 5 illustrates the steps performed at this stage.

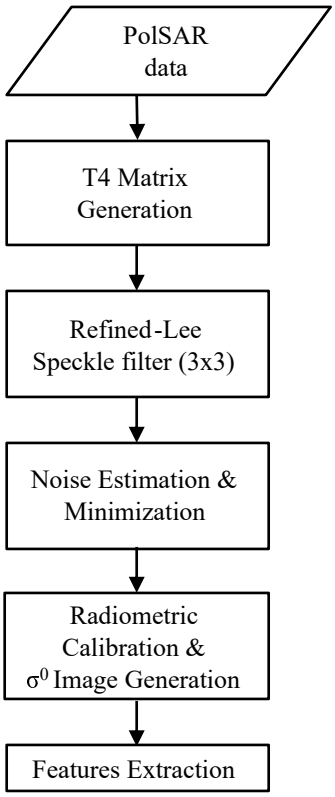

Fig. 5. Block diagram of the preprocessing scheme for features extraction.

At first, the PolSAR data were used to generate the coherency matrix T_4, which then is speckle filtered using a 3x3 refined-Lee speckle filter [30]. It is important to emphasize that, to avoid crosstalk between polarization channels, each element of the coherency matrix must be filtered independently in the spatial domain. In addition, each term should be filtered in a manner similar to multi-look processing by averaging the coherency matrix of neighboring pixels [31].

After that, the additive noise estimation and minimization are carried out. This can be achieved by diagonalizing the T_4 matrix and evaluating the eigenvalues. In the absence of noise T_4 should be of rank 3 and should have only three non-zero eigenvalues. Nonetheless, the additive noise makes T_4 to be of rank 4. In this case, the fourth eigenvalue λ_4 represents the additive noise N in the PolSAR data. Thus, the additive noise on the data can be minimized by subtracting λ_4 from the other three eigenvalues of the coherency matrix [32]. The

This work is licensed under a Creative Commons Attribution 4.0 License. For more information, see https://creativecommons.org/licenses/by/4.0/

This article has been accepted for publication in IEEE Journal of Selected Topics in Applied Earth Observations and Remote Sensing. This is the author's version which has not been fully e
content may change prior to final publication. Citation information: DOI 10.1109/JSTARS.2023.3258059

output produced in this step is then used to perform feature extraction for the machine-learning models.

B. Features Extraction and Data Preparation

A variety of disparity parameters, texture parameters, and polarimetric parameters were derived from the processed SAR data, as shown in Table IV.

TABLE IV
SUMMARY OF THE FEATURES EXTRACTED

Parameter	Description
Sigma nought	Calibrated σ^0 intensity of the HH and VV polarizations
Incidence angle	Incidence angle during data acquisition
f_2 (Contrast)	A measure of local variation
f_3 (Correlation)	A measure of the linear dependency of gray levels of neighboring pixels
f_4 (Homogeneity)	A measure of local homogeneity
f_7 (Dissimilarity)	A measure of local dissimilarity
Mean	Average between neighboring pixels
Standard deviation	Standard deviation between neighboring pixels
Entropy	Measure of the randomness of the scattering
Anisotropy	Relation between the secondary scattering processes
α	Characterizes the scattering mechanism
β	Characterizes the dominant polarization

The sigma nought σ^0 is calculated for the co-polarization and cross-polarization channels:

$$\sigma^0_{dB} = 10\log_{10}\left(|I|^2 \sin\theta_{inc}\right), \tag{3}$$

where I denotes the calibrated amplitudes of the input image, and θ_{inc} refers to the local incidence angle [28].

The texture parameters are calculated individually for each pixel, using a moving window of size 3 x 3. These features are shown in (4) to (7), where f_2, f_3, f_4, and f_7 represent, respectively, contrast, correlation, homogeneity, and dissimilarity of a Gray Level Co-occurrence Matrix (GLCM) [33], [34]. The remaining parameters obtained from the GLCM do not indicate any correlation and, therefore, are discarded from further analyses.

$$f_2 = \sum_{i,j=0}^{N-1} \left[|i-j|^2 p(i,j)\right] \tag{4}$$

$$f_3 = \frac{\sum_i \sum_j (ij)\, p(i,j) - \mu_x \mu_y}{\sigma_x \sigma_y} \tag{5}$$

$$f_4 = \sum_i \sum_j \frac{1}{1+(i-j)^2} p(i,j) \tag{6}$$

$$f_7 = \sum_i \sum_j |i-j| p(i,j) \tag{7}$$

Besides that, the mean and the standard deviation of a 3 x 3 moving window are considered. At last, the parameters entropy (H), anisotropy (A), α, and β, obtained from the Cloude-Pottier Decomposition [35], are calculated.

In statistics, two important correlation coefficients often used to measure the correlation between two variables are Pearson and Spearman [36]. Thus, after further analysis of the correlation of these variables, the parameters that do not present a direct correlation (Pearson $|r| \lesssim 0.3$) with the surface roughness previously measured are discarded. In addition, variables that show a high correlation (Spearman $|\rho| \gtrsim 0.7$) with other remaining variables are also removed, given that multicollinearity can compromise the performance of machine learning algorithms [37].

Likewise, the analysis of the Noise-Equivalent Sigma Zero (NESZ), which is a measure of the sensitivity of the SAR system to areas of low radar backscatter [38], shows that the data derived from the HV & VH channels is highly noisy, given that there is only a tiny backscatter from these channels. Therefore, the anisotropy, entropy, alpha, and other similar parameters which require the cross-polarization channels are discarded from further analysis.

As a result, the relevant features that are used as input to the machine learning models are shown in Table V.

TABLE V
SUMMARY OF THE SELECTED FEATURES

Parameter	Description
Sigma nought	Calibrated σ^0 intensity of the various available polarizations
Incidence angle	Incidence angle during data acquisition
Mean	Average between neighboring pixels
Standard deviation	Standard deviation between neighboring pixels

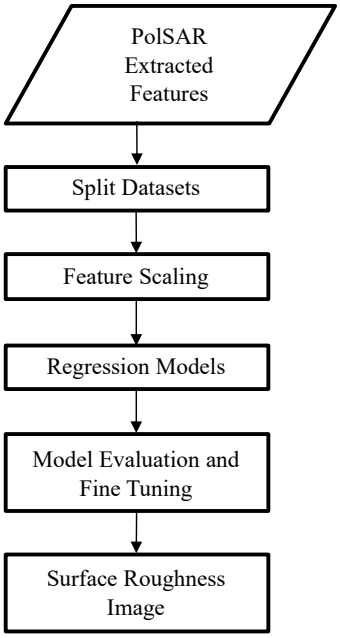

Fig. 6. Block diagram of the data pre-processing to train the machine learning models.

Finally, before performing data ingestion to train the models, it is necessary to prepare them properly. For this reason, the flowchart shown in Fig. 6 is considered. At first, the data is split into 8 datasets for training and 3 datasets for testing. After performing feature scaling, which is important to ensure that a feature with a relatively higher magnitude will not govern or control the trained model, several regression models are studied, from linear models such as linear regression to more

This work is licensed under a Creative Commons Attribution 4.0 License. For more information, see https://creativecommons.org/licenses/by/4.0/

This article has been accepted for publication in IEEE Journal of Selected Topics in Applied Earth Observations and Remote Sensing. This is the author's version which has not been fully e
content may change prior to final publication. Citation information: DOI 10.1109/JSTARS.2023.3258059

complex non-linear models, such as Artificial Neural Network (ANN), Support Vector Regression (SVR), and Random Forest Regression (RFR) [36].

C. Machine Learning Models and Techniques Used

In this subsection, the used machine learning techniques are presented in more detail, introducing the major assumptions and considerations adopted for the Support Vector Regression (SVR), Decision Trees, Random Forest Regression (RFR), and Artificial Neural Network (ANN). Moreover, the Cross Validation and Bagging techniques are presented and discussed in greater depth.

1) Support Vector Regression: A Support Vector Machine (SVM) is a powerful and versatile Machine Learning model, capable of performing linear or nonlinear classification, regression, and even outlier detection. This technique is an extension of the support vector classifier that results from enlarging the feature space using kernels, implicitly mapping their inputs into high-dimensional feature spaces [36]. The SVM can also be adapted to solve regression problems, in which case it is called Support Vector Regression. Essentially, it provides the flexibility to define how much error is acceptable in the model and it will find an appropriate line (or hyperplane in higher dimensions) to fit the data. In this research, the Radial Basis Function (RBF) kernel was adopted, which can be described by:

$$K(x, x') = e^{-\gamma \|x - x'\|} \tag{8}$$

where $\|x - x'\|$ is the squared Euclidean distance between two feature vectors (x and x') and γ is a coefficient that defines how much influence a single training example has [39]. For this work, the γ was set to $1/(n_{features}\sigma^2)$, in which σ^2 stands for the variance of X and $n_{features}$ is the number of features in the model. Moreover, another important parameter for the SVR model is the regularization parameter C, which is responsible for avoiding possible overfitting of the model. After testing several values, this parameter was set to $C = 1$ for this study.

2) Decision Trees: Decision Trees can also be applied to both regression and classification problems. Tree-based methods partition the feature space into a set of rectangles and then fit a simple model to each one. They are conceptually simple yet powerful. However, since isolated decision trees have a high variance, they typically are not competitive with the best supervised learning approaches. For this reason, decision trees are the ideal candidates for bagging [36], whose main idea is to average many noisy but relatively unbiased models, and therefore, reduce the variance.

3) Random Forest Regression: Random Forest is known as an ensemble machine learning technique that involves the creation of hundreds of decision tree models. Essentially, the Random Forest algorithm takes advantage of the bagging technique, constructing multiples of individual decision trees for each sample and averaging the results, generating a final output with reduced variance. This way, it is possible to capture complex interaction structures in the data, and if grown sufficiently deep, have relatively low bias [36], [39]. However, to prevent the trees from being too deep and to avoid overfitting, the maximum depth for the Random Forest Regression model was set to 5. Moreover, another relevant parameter in this model is the criterion (loss function) to be used during the training [36]. This parameter is responsible for measuring the quality of a split. For this work, the Mean Squared Error (MSE) was chosen, which is equal to variance reduction as a feature selection criterion.

4) Artificial Neural Network: The Artificial Neural Network (ANN), which applies both for regression and classification problems, is often represented by a network diagram as shown in Fig. 7. The basic idea behind this model is to extract linear combinations of the inputs as derived features and then model the target as a non-linear function of these resulting features [40]. For regression models, normally $K = 1$ and there is only one output unit Y_1 at the top. Derived features Z_m are created from linear combinations of the inputs X, and then the target Y_k is modeled as a function of linear combinations of the Z_m, as given by

$$\begin{aligned} Z_m &= \sigma\left(\alpha_{0m} + \alpha_m^T X\right),\ m = 1, ..., M, \\ T_k &= \beta_{0k} + \beta_k^T Z,\ k = 1, ..., K, \\ f_k(X) &= g_k(T),\ k = 1, ..., K \end{aligned} \tag{9}$$

where $Z = (Z_1, Z_2, ..., Z_M)$ and $T = (T_1, T_2, ..., T_K)$. In this equation, α_m and β_k denote the weights for the inputs X and for the hidden layers, respectively. The activation function $\sigma(v)$ is usually chosen to be the sigmoid function $\sigma(v) = 1/(1 + e - v)$ [36], [39]. In addition to the sigmoid function, there are also other activation functions broadly used in deep learning, such as logistic sigmoid, hyperbolic tangent (tanh), rectified linear units (ReLU), exponential linear unit (ELU), and scaled exponential linear unit (SELU) [40]. Finally, the output function $g_k(T)$ provides a final transformation of the outputs T. For regression problems, usually, the identity function $g_k(T) = T_k$ is adopted.

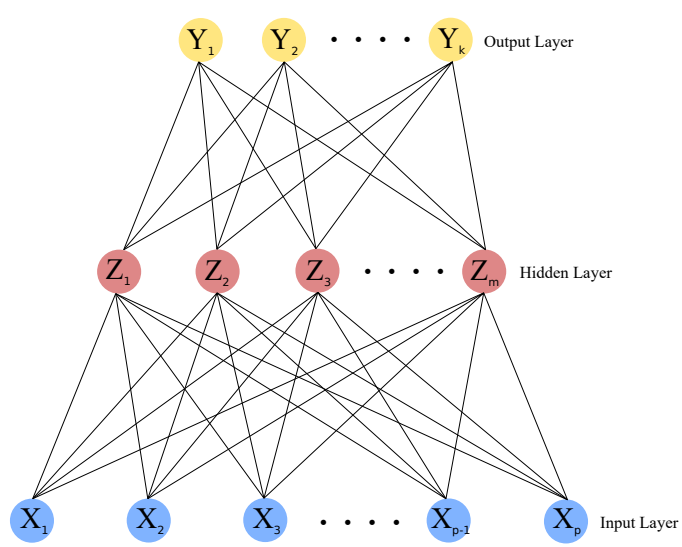

Fig. 7. Example diagram of a single-hidden-layer neural network. Adapted from [36].

This work is licensed under a Creative Commons Attribution 4.0 License. For more information, see https://creativecommons.org/licenses/by/4.0/

This article has been accepted for publication in IEEE Journal of Selected Topics in Applied Earth Observations and Remote Sensing. This is the author's version which has not been fully c
content may change prior to final publication. Citation information: DOI 10.1109/JSTARS.2023.3258059

After testing several ANN architectures, as well as comparing the performance of different activation functions, the final architecture for this model was chosen, as shown in Fig. 8. The final model is a Multi-Layer Perceptron (MLP), containing 2 hidden layers with 30 units each (without considering the bias unit). In addition, the first two layers used the Hyperbolic Tangent activation function, while the last layer used the linear function.

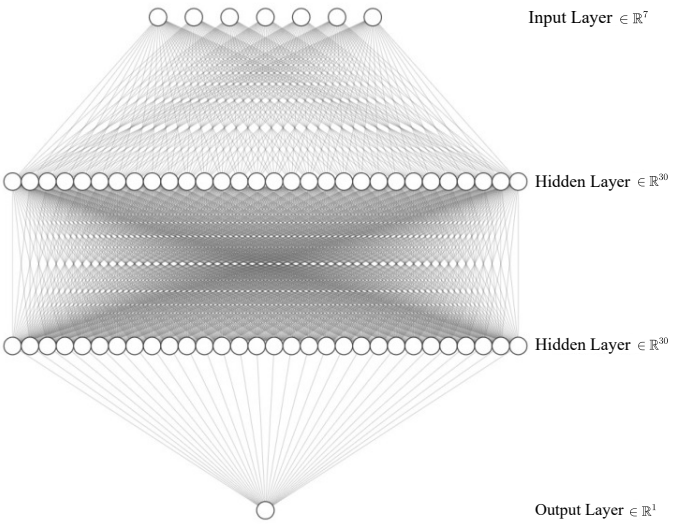

Fig. 8. Architecture chosen for the Artificial Neural Network model.

To evaluate the model's performance, the Root Mean Squared Error (RMSE) is used as a reference parameter:

$$\text{RMSE} = \sqrt{\frac{1}{n}\sum_{i=1}^{n}(\hat{y}_i - y_i)^2} \tag{10}$$

5) K-fold Cross Validation: In scenarios where the data are often scarce, it is usually not possible to separate a validation set and use it to assess the model's prediction performance. This can harm the model's efficiency since it might suffer from overfitting and therefore becoming not reliable [39]. To address this issue, techniques such as cross-validation [36] were used in order to enhance reliability and reduce the variance of the results.

The K-fold cross-validation technique uses part of the available data to fit the model and a different part to test it. The data is split into K pieces of approximately equal size. Fig. 9 illustrates a scenario in which $K = 5$. For the kth part, the model is fitted to the other $K-1$ parts of the data and calculate the prediction error of the fitted model when predicting the kth part of the data. This is done for $k = 1, 2, ..., K$ and the K estimates of prediction error are combined.

6) Bagging: Another useful technique in these scenarios is Bagging, which is a general-purpose procedure for reducing the variance of a statistical learning method. It basically consists of taking many training sets from the population, training a separate prediction model using each training set, and then averaging the resulting predictions. In other words, the bagging comprises computing $\hat{f}^1(x)$, $\hat{f}^2(x)$, ..., $\hat{f}^B(x)$

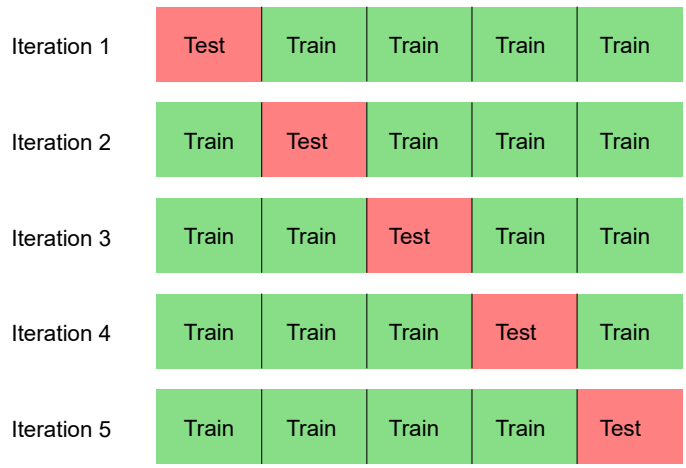

Fig. 9. Scenario example for K-fold cross-validation in which $K = 5$. Adapted from [36].

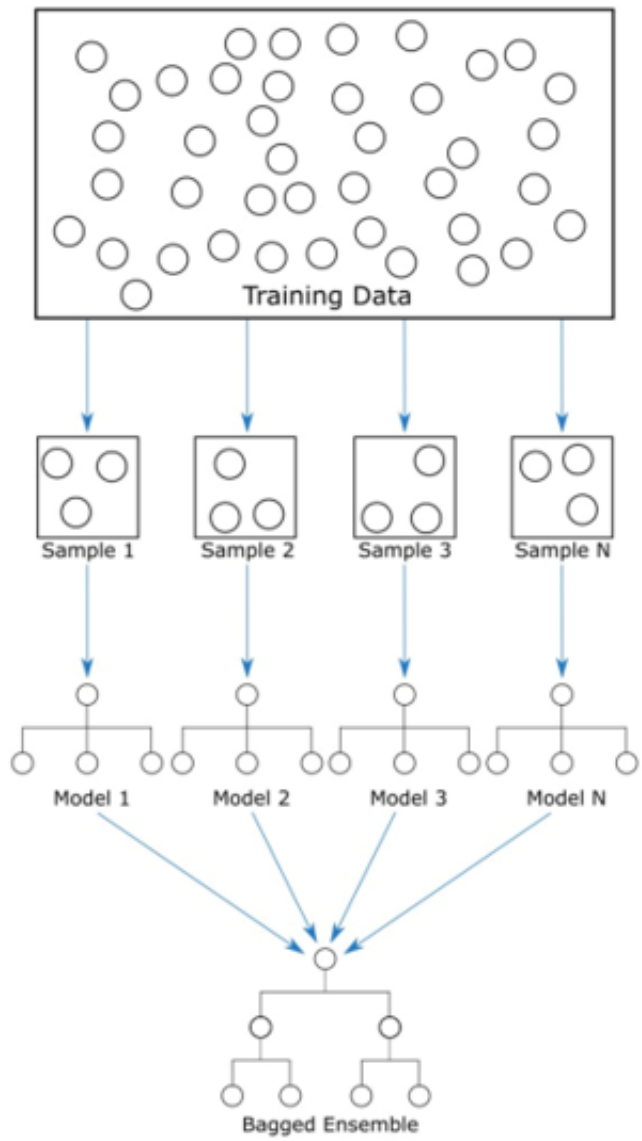

Fig. 10. Scenario example illustrating the Bagging technique.

This work is licensed under a Creative Commons Attribution 4.0 License. For more information, see https://creativecommons.org/licenses/by/4.0/

This article has been accepted for publication in IEEE Journal of Selected Topics in Applied Earth Observations and Remote Sensing. This is the author's version which has not been fully e
content may change prior to final publication. Citation information: DOI 10.1109/JSTARS.2023.3258059

using B separate training sets, and average them in order to obtain a single low-variance statistical learning model, given by $\hat{f}_{avg}(x) = \frac{1}{B}\sum_{b=1}^{B}\hat{f}^b(x)$ [36]. This architecture is illustrated in Fig. 10.

V. Experimental Results and Discussion

This section discusses the surface roughness estimation results obtained using the methods described in the previous section.

To validate the surface roughness results obtained from the machine learning models, the results must be compared to the ground-truth surface roughness values as well as to the surface roughness results obtained from the roughness estimation models commonly used in the literature. However, as already mentioned in the introduction section of this article, these models are originally developed for agricultural lands and are not suitable for a road surface. This can be further verified by analyzing the σ^0 and NESZ values on the road surfaces.

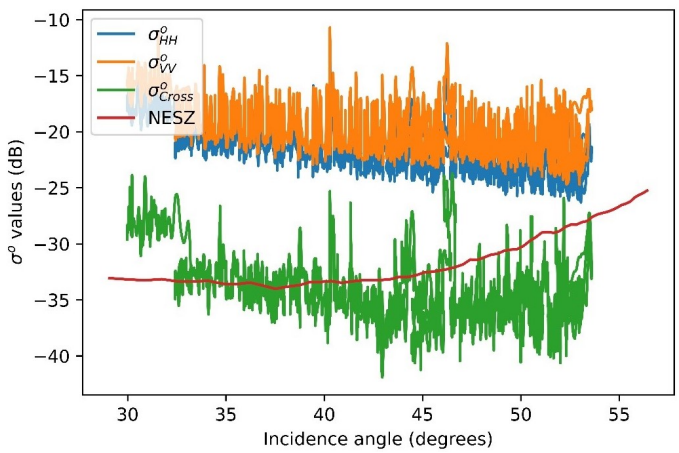

Fig. 11. σ^0 and NESZ plots for the Kaufbeuren runway

Fig. 11 shows the σ^0 and NESZ plots for the Kaufbeuren runway. The values are plotted from one end of the runway to the other for the F-SAR PS05 dataset where the runway is along range direction. Therefore, the incidence angle increases from one end of the runway to the other. In Fig. 11, the blue represents the σ^0 values in HH polarization, the orange in VV polarization, the green represents the cross-polarized σ^0 values, and the red shows the NESZ as a function of incidence angle. It can be seen that the σ^0 values for HH and VV co-polarizations stay above the NESZ level even at shallow incidence angles. This means that the backscattered signal from the roads in the co-polarization channels is above the noise floor of the SAR system. On the other hand, the cross-polarized σ^0 data (green plot) fall below the NESZ level for the road surface as the incidence angle increases. This means that the backscattered signal from the roads in the cross-polarization channels is dominated by noise and is not suitable for estimating road surface roughness. As mentioned in the methodology section, this is the reason why HV and VH cross-polarization channels are not used as input to the machine learning models. The SAR polarimetry-based models [17] and the Oh models [18], [19] used in the literature for roughness estimation require the cross-polarization channels and hence cannot be used for road surface roughness estimation. The remaining models that require only the co-polarization channels are the semi-empirical Dubois model [20] and the modified Dubois model specifically developed for the road surface roughness estimation [24]. In [24], it was shown that the Dubois model has an incidence angle dependency and cannot estimate the roughness changes between concrete and asphalt surfaces at steeper incidence angles, which led to the development of the modified Dubois model for road surface roughness estimation. Therefore, the surface roughness results obtained with the machine learning models are compared with the modified Dubois model from [24].

At the primary test site in Kaufbeuren, the results were compared with the ground-truth values as well as with the modified Dubois model. On the other hand, in the secondary test sites, the results were only compared to the modified Dubois model results, since there is no ground-truth data available.

A. Kaufbeuren Test Site

After training the SVR, RFR, and ANN models with the eight training datasets (cf. Table II), these models were then applied to the three test datasets for calculating the road surface roughness (h_{rms}) values. For evaluating the performance of these models, the h_{rms} values were estimated for the GT spots. Then the RMSE between the model estimated h_{rms} and GT h_{rms} values were calculated for both the train and test datasets. The GT spot 9 was not used in this analysis due to a severe crack causing a bias. Moreover, the GT spot 10 was also left out of the analysis because the system did not receive a strong enough signal from it, resulting in a low signal-to-noise ratio (SNR).

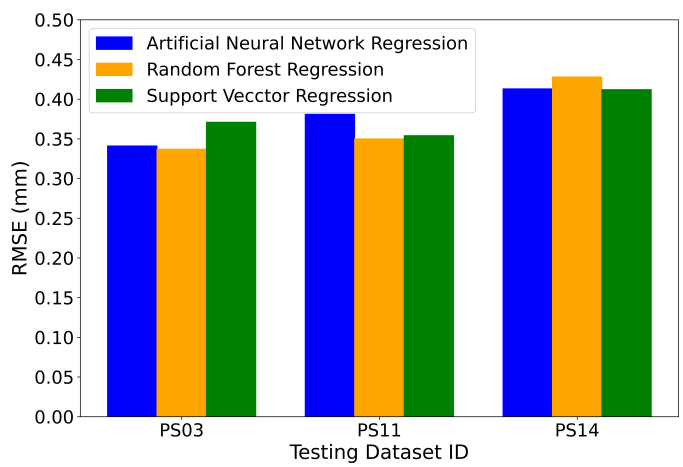

Fig. 12. RMSE values estimated from the test datasets for the machine learning models at the Kaufbeuren runway test site.

Fig. 12 shows the RMSE values obtained for the SVR, RFR, and ANN models from the three test datasets. For the PS03 dataset, which has a 45° flight track w.r.t. the Kaufbeuren runway, the RFR model has the lowest RMSE of 0.33 mm. The highest RMSE of 0.37 mm is observed for the SVR model.

This work is licensed under a Creative Commons Attribution 4.0 License. For more information, see https://creativecommons.org/licenses/by/4.0/

This article has been accepted for publication in IEEE Journal of Selected Topics in Applied Earth Observations and Remote Sensing. This is the author's version which has not been fully e
content may change prior to final publication. Citation information: DOI 10.1109/JSTARS.2023.3258059

For the PS11 dataset, which was acquired with a flight track parallel to the runway and also with an incidence angle of approximately 39° at the runway, the RFR model has the lowest RMSE of 0.35 mm and the highest RMSE of 0.38 mm is obtained for the ANN model. The PS14 dataset was also acquired with a flight track parallel to the runway and with an incidence angle of approximately 45° at the runway. For this dataset, the lowest RMSE of 0.41 mm was observed for the SVR model and the highest RMSE of 0.43 mm was observed for the RFR model.

From Fig. 12, it can be seen that the RMSE for the models varies depending on the datasets. However, from all test datasets and models, it can be seen that the lowest RMSE is 0.33 mm and the highest RMSE is 0.43 mm, which is not a large variation. Table VI summarizes the mean RMSE values, by taking the mean from multiple datasets for both the training set and the test set. It can be seen that for the training set, the lowest RMSE is 0.32 mm for the SVR model and the highest RMSE is 0.36 mm for the RFR model. In the case of the test set, the lowest RMSE of 0.37 mm is obtained for the ANN model and the highest RMSE of 0.39 mm is obtained for both the SVR and RFR models. It can be seen from both Fig. 12 and Table VI that the RMSE variations for all the models are very low, which shows the consistency of the models in estimating the h_{rms} values.

TABLE VI
MEAN RMSE FOR BOTH THE TRAINING AND TEST DATASETS AT THE KAUFBEUREN TEST SITE

Model	RMSE Training [mm]	RMSE Test [mm]
Artificial Neural Network (ANN)	0.35	0.37
Support Vector Regression (SVR)	0.32	0.39
Random Forest Regression (RFR)	0.36	0.39

Fig. 13 and Fig. 14 show the surface roughness (h_{rms}) images generated from the PS14 and PS03 test datasets, respectively. As mentioned before, the PS14 dataset was acquired with a flight track parallel to the runway with an incidence angle of approximately 45°, and the PS03 dataset was acquired with a 45° flight track w.r.t. the runway and the incidence angle varies from 29° to 55° from one end of the runway to the other. Figs. 13(a) and 14(a) were generated using the ANN model, Figs. 13(b) and 14(b) using the SVR model. The RFR model results are shown in Figs. 13(c) and 14(c). It is important to note that in these figures the areas outside the runway, taxiway, and parking space are not valid, but were not cut out since no geocoding was done.

Fig. 15 shows the h_{rms} generated using the modified Dubois model for the PS03 dataset. In contrast to Fig. 13 and Fig. 14, this image was geocoded and had the irrelevant regions removed. By comparing all the h_{rms} images shown in Fig. 13 and Fig. 14 with Fig. 15, it can be seen that the h_{rms} images generated by the ANN, SVR, and RFR models are matching with the h_{rms} image generated by the modified Dubois model. In all the images, the asphalt regions are appearing primarily in blue color indicating roughness values in the 0.5 to 1.0 mm range. The concrete regions at both ends of the runway are appearing in yellow color indicating higher surface roughness in the 1.0 to 1.5 mm range. Also, the concrete areas with cuts on the top end of the runway are appearing in green color indicating higher roughness (1.5 to 2.0 mm range) compared to the other concrete regions without cuts. This is more evident in the PS03 dataset due to its 45° flight track to the runway which resulted in more backscattering from the cuts in the concrete. By further comparing the results with Fig. 3 and Table. III, it can be observed that the ANN, SVR, and RFR models were able to distinguish the different compositions in the runway structure.

TABLE VII
COMPARISON OF SURFACE ROUGHNESS RESULTS AT GT SPOTS BY AVERAGING MULTIPLE DATASETS

GT spot	GT h_{rms} (mm)	Modif. Dubois Model	ANN Model	SVR Model	RFR Model
1	2.36	1.78	1.50	1.42	1.37
2	0.99	1.14	1.09	1.05	1.10
3	0.66	0.60	0.69	0.68	0.72
4	0.88	1.40	1.29	1.32	1.26
5	0.68	0.80	1.00	0.89	0.77
6	0.98	0.79	0.93	0.82	0.79
7	1.09	1.28	1.30	1.31	1.21
8	0.61	0.59	0.65	0.69	0.72
RMSE (mm)		0.299	0.365	0.388	0.389

Additionally, Table VII lists the h_{rms} values estimated at each ground-truth spot for each model examined in this study. The obtained surface roughness from this investigation was calculated by taking the average of three test datasets. By comparing the results, it can be seen that the machine learning models were consistent with the modified Dubois model, dis-

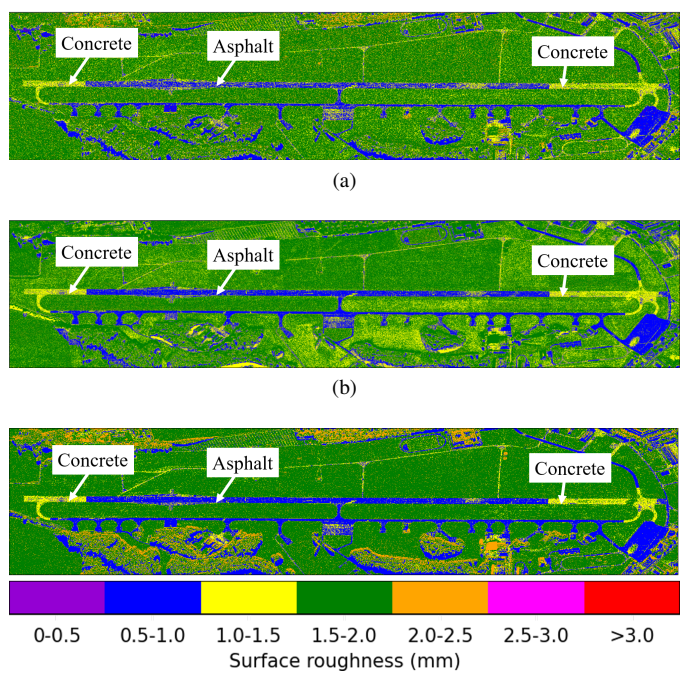

Fig. 13. Surface roughness images obtained from Kaufbeuren test datasets for several regression models. (a) Artificial Neural Network. (b) Support Vector Regression. (c) Random Forest Regression.

This work is licensed under a Creative Commons Attribution 4.0 License. For more information, see https://creativecommons.org/licenses/by/4.0/

This article has been accepted for publication in IEEE Journal of Selected Topics in Applied Earth Observations and Remote Sensing. This is the author's version which has not been fully e
content may change prior to final publication. Citation information: DOI 10.1109/JSTARS.2023.3258059

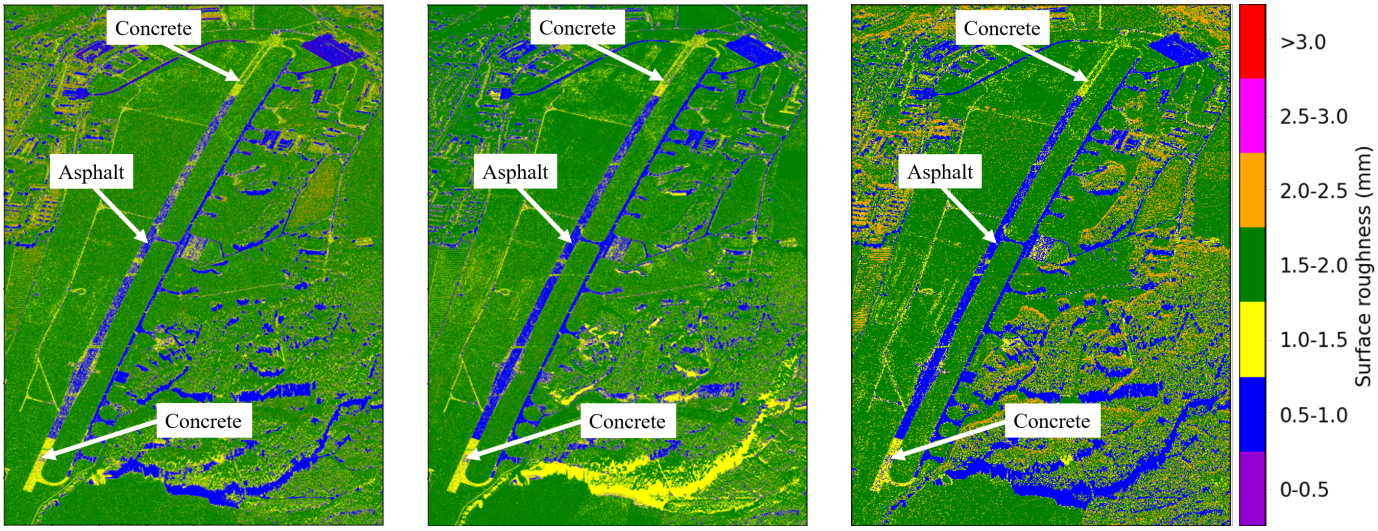

(a) (b) (c)

Fig. 14. Surface roughness image obtained from an alternative Kaufbeuren test dataset for several regression models. (a) Artificial Neural Network. (b) Support Vector Regression. (c) Random Forest Regression.

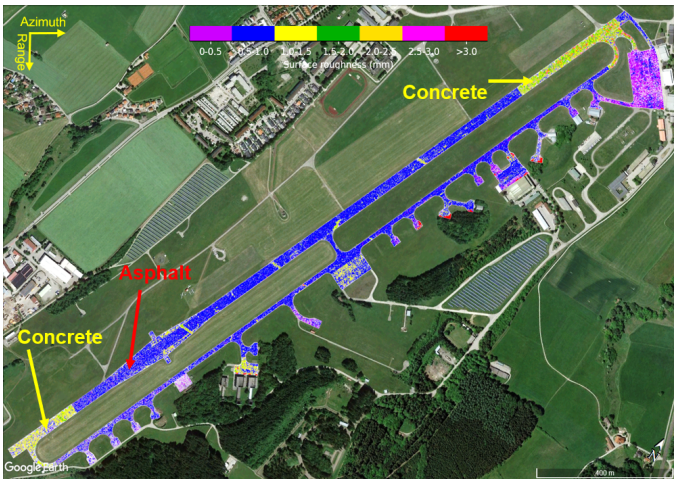

Fig. 15. Kaufbeuren surface roughness image for the modified Dubois model [24].

playing similar results. Moreover, among the machine learning models, although the Random Forest Regression did not have the lowest RMSE value, it achieved the best result. In fact, this can be seen in the surface roughness images (Fig. 13(c) and Fig. 14(c)), in which this model presented the lowest noise when compared to the others.

B. DuraBASt Test Site

Likewise, the h_{rms} images generated using the ANN, SVR, and RFR models for the duraBASt test site are shown in Fig. 16. This test site proved to be much noisier than the previous one. This happens because, unlike the previous test site, there is intense vehicle traffic in the region, which interferes with the data obtained by the SAR. In the same way, the vegetation close to the highway also generates shadow regions harming the model's performance [41].

Nonetheless, it is still possible to compare the performance of the models with the modified Dubois model. The h_{rms} images generated using the ANN, SVR, and RFR models are shown in Figs. 16(a), (b), and (c), respectively. Fig. 16(d) shows the h_{rms} image generated using the modified Dubois model. It can be seen that the surface roughness results estimated by the ANN, SVR, and RFR models are matching with the modified Dubois model result. The smooth areas on the duraBASt test site are appearing in blue color indicating low surface roughness and the rougher regions are appearing in yellow color indicating higher values of surface roughness. In addition, a sudden change in surface roughness can be noticed in the nearby highway indicated by the color change from blue to yellow and green, which is probably due to a different material composition. In fact, also the optical image in Fig. 16(e) shows a change in the appearance of the road surface in the smooth and rough regions both on the duraBASt test site and on the highway.

C. Wolfsburg Motorway Intersection, Braunschweig

The h_{rms} images for the Braunschweig motorway test site are shown in Fig. 17. Fig. 17(a) shows the h_{rms} result from the ANN model, Fig. 17(b) from the SVR model, the h_{rms} estimated using the RFR model is shown in Fig. 17(c). It can be seen that most parts of the motorway are appearing in blue color indicating h_{rms} values in the range of 0.5 mm to 1.0 mm. However, in the area shown in the detailed view, a sudden change in color from blue to yellow can be observed which indicates a higher surface roughness in the range of 1.0 to 1.5 mm range. Similar to the duraBASt test site, this sudden change in surface roughness may also be due to the use of materials with different compositions during a maintenance activity. Again, the ANN, SVR, and RFR models proved capable of distinguishing the different compositions on the road. Moreover, it can be seen that the results obtained by

This work is licensed under a Creative Commons Attribution 4.0 License. For more information, see https://creativecommons.org/licenses/by/4.0/

This article has been accepted for publication in IEEE Journal of Selected Topics in Applied Earth Observations and Remote Sensing. This is the author's version which has not been fully c
content may change prior to final publication. Citation information: DOI 10.1109/JSTARS.2023.3258059

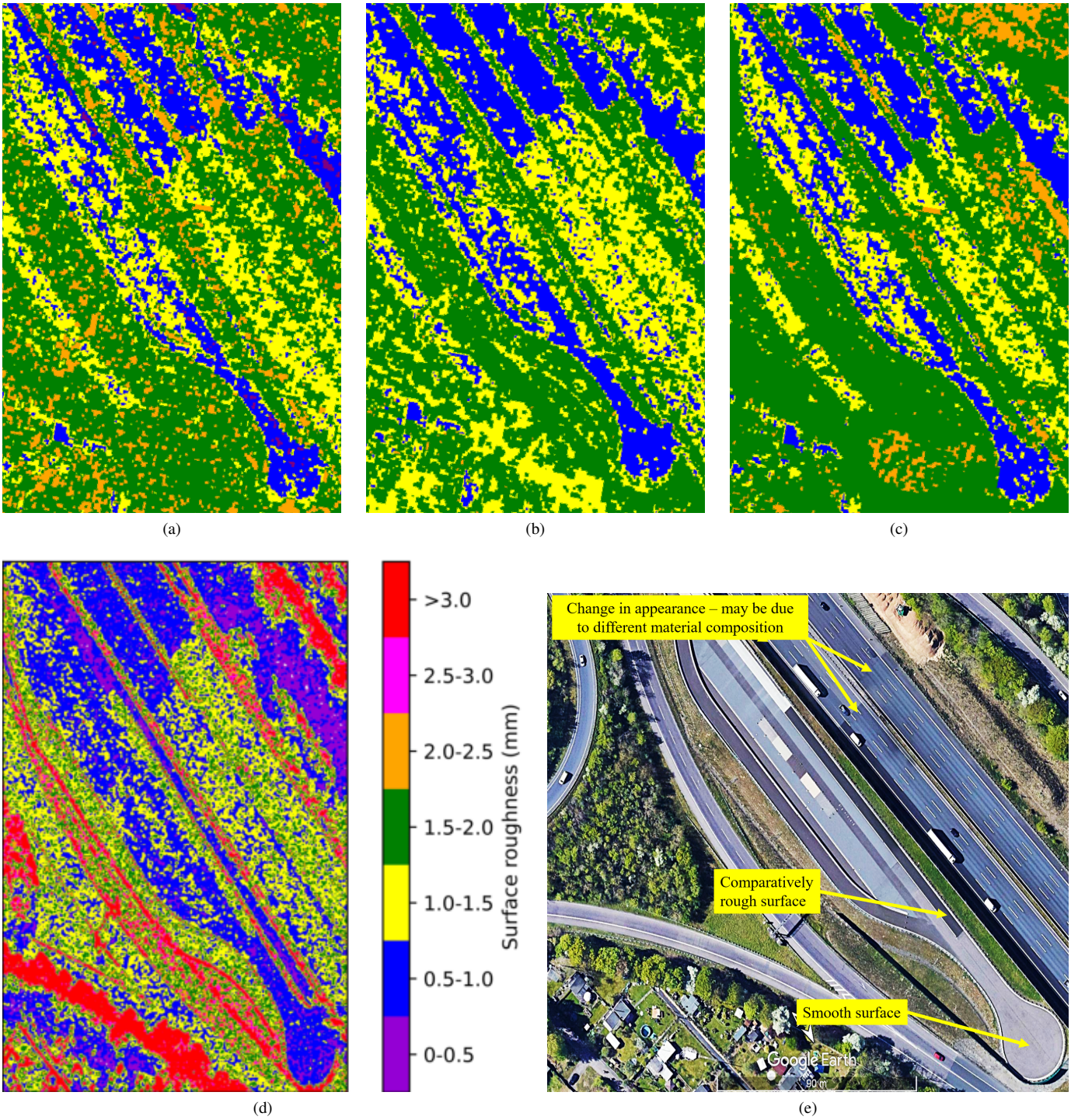

Fig. 16. Surface roughness results for the duraBASt test site, with results obtained using (a) Artificial Neural Network, (b) Support Vector Regression, (c) Random Forest Regression, and (d) Modified Dubois model. (e) Corresponding Google-Earth image.

This work is licensed under a Creative Commons Attribution 4.0 License. For more information, see https://creativecommons.org/licenses/by/4.0/

This article has been accepted for publication in IEEE Journal of Selected Topics in Applied Earth Observations and Remote Sensing. This is the author's version which has not been fully e
content may change prior to final publication. Citation information: DOI 10.1109/JSTARS.2023.3258059

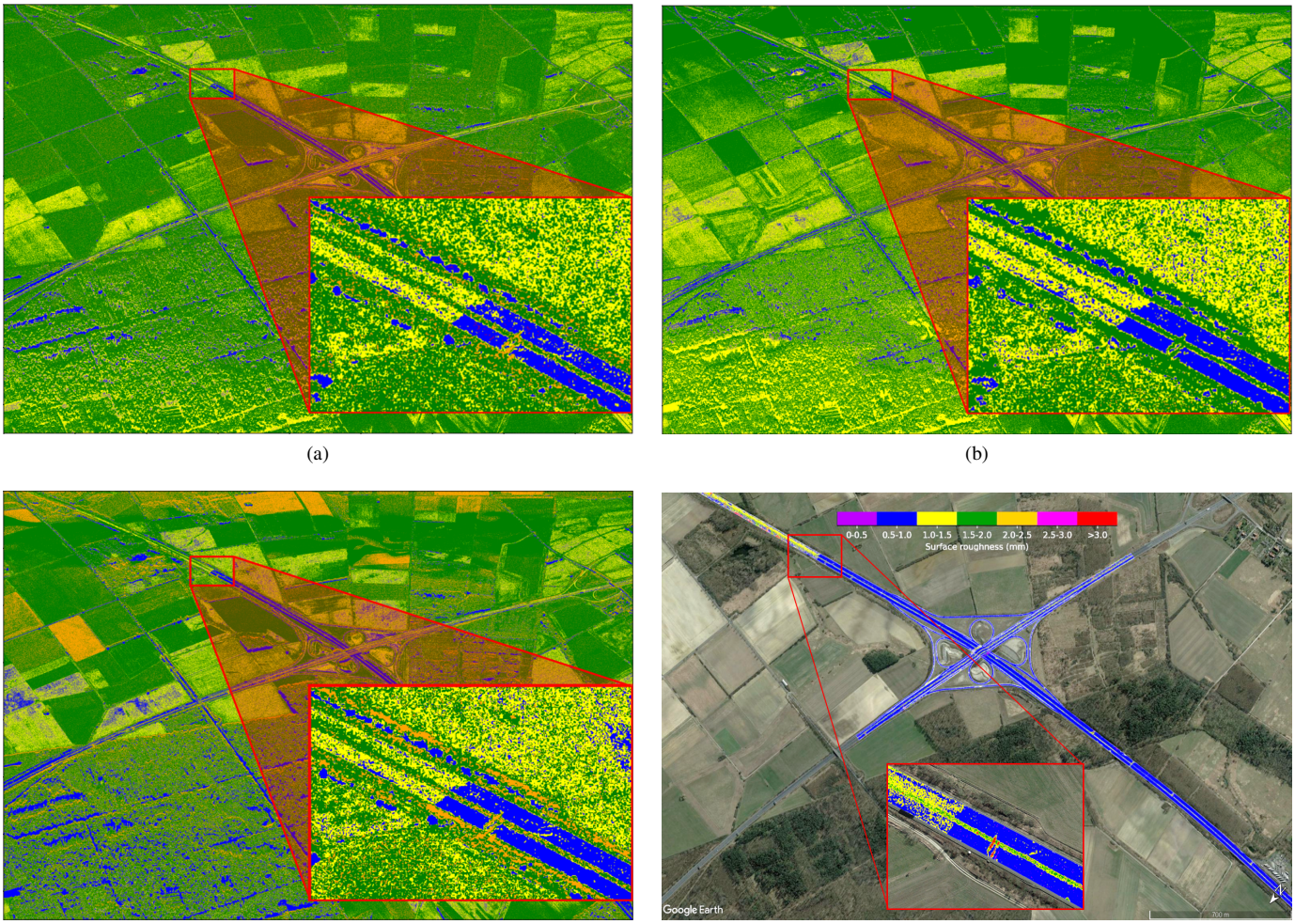

(a) (b) (c) (d)

Fig. 17. Braunschweig motorway surface roughness images obtained with different regression models. (a) Artificial Neural Network. (b) Support Vector Regression. (c) Random Forest Regression. (d) Modified Dubois model.

the machine learning models are consistent with the result generated by the modified Dubois model (Fig. 17(d)).

VI. Conclusion

This paper proposes a new machine learning-based approach for monitoring road surface roughness using a fully polarimetric airborne SAR system. It was shown that the used X-band data have a good sensitivity in relation to the road surface roughness and, therefore, present a high potential to estimate the surface roughness in a fast and efficient way. Furthermore, it was observed that the low radar backscatter obtained from the smooth road surface complicates the estimation process and it is initially necessary to minimize the additive noise in the datasets. Moreover, the cross-polarized channels proved to be very noisy, thus the parameters and models dependent on these channels showed to be unreliable. Despite the challenges due to the additive noise and the shadow regions, the results of the machine learning models are consistent with the results of the recently introduced modified Dubois model [24] and the ground truth data, showing good potential for further research. It is worth noting that the semi-empirical modified Dubois model still gives slightly better results, and is also more computationally efficient and faster compared to machine learning-based models. However, the performance of the semi-empirical model is limited to the validity range and other conditions assumed during its development. On the other hand, machine learning models can adapt to variations in data and environments. Therefore, the semi-empirical modified Dubois model can be a good option for road surface roughness estimation when the input data meets the model's validity conditions. In other situations, machine learning-based models may be more suitable for better road surface roughness estimation. In future studies, further experiments using other bands, such as the Ka-band, could improve the roughness estimation results significantly. Currently we are investigating high-resolution X-band SAR data acquired with the German TerraSAR-X radar satellite to determine if even in the spaceborne case the SNR is high enough for a reliable road surface roughness estimation. The first results are promising and will be published in a follow-up paper.

This work is licensed under a Creative Commons Attribution 4.0 License. For more information, see https://creativecommons.org/licenses/by/4.0/

This article has been accepted for publication in IEEE Journal of Selected Topics in Applied Earth Observations and Remote Sensing. This is the author's version which has not been fully e
content may change prior to final publication. Citation information: DOI 10.1109/JSTARS.2023.3258059

REFERENCES

[1] X. Zhang, "Transport infrastructure, spillover and regional economic growth," *Nanjing: Nanjing*, 2009.

[2] Y. Zhou, C. Tong, and Y. Wang, "Road construction, economic growth, and poverty alleviation in china," *Growth and Change*, vol. 53, no. 3, pp. 1306–1332, 2022.

[3] J. Hofmockel, J. Masino, J. Thumm, E. Sax, and F. Gauterin, "Multiple vehicle fusion for a robust road condition estimation based on vehicle sensors and data mining," *Cogent Engineering*, vol. 5, no. 1, p. 1449428, 2018.

[4] G. Porter, "Transport services and their impact on poverty and growth in rural sub-saharan africa: A review of recent research and future research needs," *Transport reviews*, vol. 34, no. 1, pp. 25–45, 2014.

[5] A. Babu and S. V. Baumgartner, "Road surface roughness estimation using polarimetric sar data," in *2020 21st International Radar Symposium (IRS)*, 2020, pp. 281–285.

[6] R. Ghandour, A. Victorino, M. Doumiati, and A. Charara, "Tire/road friction coefficient estimation applied to road safety," in *18th Mediterranean Conference on Control and Automation, MED'10*, 2010, pp. 1485–1490.

[7] P. Wriggers and J. Reinelt, "Multi-scale approach for frictional contact of elastomers on rough rigid surfaces," *Computer Methods in Applied Mechanics and Engineering*, vol. 198, no. 21, pp. 1996–2008, 2009, advances in Simulation-Based Engineering Sciences – Honoring J. Tinsley Oden.

[8] H. Liu, Z. Zhang, D. Guo, L. Peng, Z. Bao, and W. Han, "Research progress on characteristic technique of pavement micro-texture and testing technology of pavement skid resistance at home and abroad," in *2011 International Conference on Remote Sensing, Environment and Transportation Engineering*, 2011, pp. 4368–4372.

[9] M. Acosta, S. Kanarachos, and M. Blundell, "Road friction virtual sensing: A review of estimation techniques with emphasis on low excitation approaches," *Applied Sciences*, vol. 7, no. 12, 2017.

[10] Q. Li, F. Qiao, and L. Yu, "Impacts of pavement types on in-vehicle noise and human health," *Journal of the Air & Waste Management Association*, vol. 66, no. 1, pp. 87–96, 2016, pMID: 26569334.

[11] E. Parliament, D.-G. for Internal Policies of the Union, A. Stanghellini, R. Frisoni, R. Lidia, J. Neri, T. Sawicki, L. Devenish, L. Casullo, S. Carl, C. Vollath, R. Silaghi, F. Spano, and F. Dionori, *EU road surfaces : economic and safety impact of the lack of regular road maintenance*. Publications Office, 2014.

[12] K. Laubis, "Crowd-based road surface monitoring and its implications on road users and road authorities," Ph.D. dissertation, Karlsruher Institut für Technologie (KIT), 2019.

[13] M. I. Bani Baker, R. M. Abendeh, and M. A. Khasawneh, "Freeze and thaw effect on asphalt concrete mixtures modified with natural bentonite clay," *Coatings*, vol. 12, no. 11, 2022.

[14] F. Ulaby, D. Long, U. of Michigan. Press, C. Elachi, and K. Sarabandi, *Microwave Radar and Radiometric Remote Sensing*. University of Michigan Press, 2014.

[15] R. S. Dwivedi, B. R. Rao, and S. P. Kushwaha, "The utility of day-and-night observation and cloud-penetration capability of ers-1 sar data for detection of wetlands," *Geocarto International*, vol. 15, no. 1, pp. 7–12, 2000.

[16] N. Baghdadi, M. El Hajj, M. Choker, M. Zribi, H. Bazzi, E. Vaudour, J.-M. Gilliot, and D. M. Ebengo, "Potential of sentinel-1 images for estimating the soil roughness over bare agricultural soils," *Water*, vol. 10, no. 2, 2018.

[17] I. Hajnsek, "Inversion of surface parameters using polarimetric sar," Ph.D. dissertation, Friedrich Schiller University Jena, 2001.

[18] Y. Oh, K. Sarabandi, and F. Ulaby, "An empirical model and an inversion technique for radar scattering from bare soil surfaces," *IEEE Transactions on Geoscience and Remote Sensing*, vol. 30, no. 2, pp. 370–381, 1992.

[19] Y. Oh, "Quantitative retrieval of soil moisture content and surface roughness from multipolarized radar observations of bare soil surfaces," *IEEE Transactions on Geoscience and Remote Sensing*, vol. 42, no. 3, pp. 596–601, 2004.

[20] P. Dubois, J. van Zyl, and T. Engman, "Measuring soil moisture with imaging radars," *IEEE Transactions on Geoscience and Remote Sensing*, vol. 33, no. 4, pp. 915–926, 1995.

[21] W. Suanpaga and K. Yoshikazu, "Riding quality model for asphalt pavement monitoring using phase array type l-band synthetic aperture radar (palsar)," *Remote Sensing*, vol. 2, no. 11, pp. 2531–2546, 2010.

[22] S.-L. Chen, C.-H. Lin, C.-W. Tang, L.-P. Chu, and C.-K. Cheng, "Research on the international roughness index threshold of road rehabilitation in metropolitan areas: A case study in taipei city," *Sustainability*, vol. 12, no. 24, 2020.

[23] F. J. Meyer, O. A. Ajadi, and E. J. Hoppe, "Studying the applicability of x-band sar data to the network-scale mapping of pavement roughness on us roads," *Remote Sensing*, vol. 12, no. 9, 2020.

[24] A. Babu, S. V. Baumgartner, and G. Krieger, "Approaches for Road Surface Roughness Estimation Using Airborne Polarimetric SAR," *IEEE Journal of Selected Topics in Applied Earth Observations and Remote Sensing*, vol. 15, pp. 3444–3462, Apr. 2022.

[25] I. H. Sarker, "Machine learning: Algorithms, real-world applications and research directions," *SN Computer Science*, vol. 2, no. 3, p. 160, Mar 2021.

[26] Federal Highway Research Institute, "BASt special," in *Research Controlling and Press and Public Relations, Bergisch Gladbach*, 2017.

[27] A. Babu and S. V. Baumgartner, "Road surface quality assessment using polarimetric airborne sar," in *2020 IEEE Radar Conference (RadarConf20)*, 2020, pp. 1–5.

[28] M. Keller, J. Fischer, and M. Jager, "DLR's Airborne SAR F-SAR Product Description." Microwaves and Radar Institute, German Aerospace Center, Oberpfaffenhofen, 2019.

[29] R. Horn, M. Jaeger, M. Keller, M. Limbach, A. Nottensteiner, M. Pardini, A. Reigber, and R. Scheiber, "F-sar - recent upgrades and campaign activities," in *2017 18th International Radar Symposium (IRS)*, 2017, pp. 1–10.

[30] A. S. Yommy, R. Liu, Wu, and Shuang, "Sar image despeckling using refined lee filter," in *2015 7th International Conference on Intelligent Human-Machine Systems and Cybernetics*, vol. 2, 2015, pp. 260–265.

[31] J.-S. Lee, M. Grunes, and G. de Grandi, "Polarimetric sar speckle filtering and its implication for classification," *IEEE Transactions on Geoscience and Remote Sensing*, vol. 37, no. 5, pp. 2363–2373, 1999.

[32] I. Hajnsek, K. Papathanassiou, and S. Cloude, "Removal of additive noise in polarimetric eigenvalue processing," in *IGARSS 2001. Scanning the Present and Resolving the Future. Proceedings. IEEE 2001 International Geoscience and Remote Sensing Symposium (Cat. No.01CH37217)*, vol. 6, 2001, pp. 2778–2780 vol.6.

[33] R. M. Haralick, K. Shanmugam, and I. Dinstein, "Textural features for image classification," *IEEE Transactions on Systems, Man, and Cybernetics*, vol. SMC-3, no. 6, pp. 610–621, 1973.

[34] L.-K. Soh and C. Tsatsoulis, "Texture analysis of sar sea ice imagery using gray level co-occurrence matrices," *IEEE Transactions on Geoscience and Remote Sensing*, vol. 37, no. 2, pp. 780–795, 1999.

[35] S. Cloude and E. Pottier, "A review of target decomposition theorems in radar polarimetry," *IEEE Transactions on Geoscience and Remote Sensing*, vol. 34, no. 2, pp. 498–518, 1996.

[36] T. Hastie, R. Tibshirani, and J. Friedman, *The Elements of Statistical Learning*, 08 2009.

[37] A. Alin, "Multicollinearity," *WIREs Computational Statistics*, vol. 2, no. 3, pp. 370–374, 2010. [Online]. Available: https://wires.onlinelibrary.wiley.com/doi/abs/10.1002/wics.84

[38] M. Younis, S. Huber, P. Anton, F. Bordoni, and G. Krieger, "Performance comparison of reflector- and planar-antenna based digital beam-forming sar," *International Journal of Antennas and Propagation*, vol. 2009, 01 2009.

[39] A. Geron, *Hands-on machine learning with scikit-learn, keras, and TensorFlow*, 2nd ed. Sebastopol, CA: O'Reilly Media, Oct. 2019.

[40] I. Goodfellow, Y. Bengio, and A. Courville, *Deep Learning*, ser. Adaptive Computation and Machine Learning series. London, England: MIT Press, Nov. 2016.

[41] A. M. Raynal and D. L. Bickel, "Imaging radar performance analysis using product dark regions," in *Radar Sensor Technology XXII*, K. I. Ranney and A. Doerry, Eds., vol. 10633, International Society for Optics and Photonics. SPIE, 2018, pp. 319 – 329. [Online]. Available: https://doi.org/10.1117/12.2309372

This work is licensed under a Creative Commons Attribution 4.0 License. For more information, see https://creativecommons.org/licenses/by/4.0/